

# Emergence of a metallic metastable phase induced by electrical current in $\text{Ca}_2\text{RuO}_4$

C. Cirillo<sup>1</sup>, V. Granata<sup>2</sup>, G. Avallone<sup>2</sup>, R. Fittipaldi<sup>1</sup>, C. Attanasio<sup>2</sup>, A. Avella<sup>2</sup> and A. Vecchione<sup>1</sup>

<sup>1</sup>CNR-SPIN, c/o Università degli Studi di Salerno - Via Giovanni Paolo II, 132 - I-84084 - Fisciano (Sa), Italy

<sup>2</sup>Dipartimento di Fisica “E.R. Caianiello”, Università degli Studi di Salerno - Via Giovanni Paolo II, I-84084 Fisciano (Sa), Italy



(Received 25 July 2019; revised manuscript received 2 December 2019; published 27 December 2019)

A comprehensive study of the behavior of the Mott insulator  $\text{Ca}_2\text{RuO}_4$  under electrical current drive is performed by combining two experimental probes: the macroscopic electrical transport and the microscopic x-ray diffraction. The resistivity,  $\rho$ , versus electric current density,  $J$ , and temperature,  $T$ ,  $\rho(J, T)$ , resistivity map is drawn. In particular, the metastable state, induced between the insulating and the metallic thermodynamic states by current biasing  $\text{Ca}_2\text{RuO}_4$  single crystals, is investigated. Such an analysis, combined with the study of the resulting  $\text{RuO}_6$  octahedra energy levels, reveals that a metallic crystal phase emerges in the metastable regime. The peculiar properties of such a phase, coexisting with the well-established orthorhombic insulating and tetragonal metallic phases, allow one to explain some of the unconventional and puzzling behaviors observed in the experiments as a negative differential resistivity.

DOI: [10.1103/PhysRevB.100.235142](https://doi.org/10.1103/PhysRevB.100.235142)

## I. INTRODUCTION

$\text{Ca}_2\text{RuO}_4$  (hereafter Ca-214) is a paramagnetic Mott insulator, the subject of extensive experimental and theoretical studies [1–5]. The richness of its phase diagram [2,6] and the strong interplay between electronic, structural, magnetic and orbital degrees of freedom make the full comprehension of the physics of this system challenging [1,4,7,8]. This material indeed exhibits very different responses, both in the magnetic and transport properties, to different combinations of temperature [9,10], pressure [6,11,12], doping [3,13,14], and electrical field [15].

Ca-214 is a layered perovskite oxide with  $Pbca$  space-group symmetry whose crystallographic unit cell contains four formula units [see Fig. 1(a)]. The fundamental structural units are  $\text{RuO}_6$  octahedra arranged in corner-shared planes alternated by layers containing the Ca atoms. With respect to the ideal tetragonal structure (with lattice parameters  $a = b$ ,  $c$ ), the octahedra bear alternating rotations (about the apical Ru-O2 bond;  $z$  hereafter), tilts (of  $z$  with respect to the  $ab$  plane initially containing the Ru-O1 bonds;  $x$  and  $y$  hereafter), and distortions (making  $x$  and  $y$  slightly different) [16] (see Appendices). The ratios between  $x$  and  $y$  and, in particular, between their average,  $\bar{x}$ , and  $z$  determine the relative energies of the  $t_{2g}$  orbitals of Ru ( $d_{xy}$ ,  $d_{yz}$ ,  $d_{xz}$ ), which are the electrons responsible for transport as well as all other response properties.  $x/y$  rules the relative position of  $d_{yz}$  and  $d_{xz}$  levels while  $z/\bar{x}$  rules the relative position of  $d_{xy}$  with respect to the  $d_{yz}$ - $d_{xz}$  doublet (see Appendices).

As schematically shown in Fig. 1(b), these ratios change with the temperature,  $T$ . In particular,  $z/\bar{x}$  increases with  $T$ , as  $c/\bar{a}$  does ( $\bar{a}$  is the average between  $a$  and  $b$ ). For temperatures below  $T_{\text{AFM}} \approx 110$  K, the ratio is lower than 1. As a consequence, the system is an antiferromagnetic (AFM) insulator [9] with  $d_{xy}$  lower than  $d_{yz}$ - $d_{xz}$  doublet and the four electrons per Ru atom arranged as shown in Fig. 1(c) (I-short). At intermediate and ambient  $T$ ,  $z/\bar{x}$  goes through

about 1, which results in a paramagnetic strongly correlated Mott insulator (I-SC) with the three levels almost degenerate (M), before both  $d_{yz}$  and  $d_{xz}$  go through a Mott-Hubbard splitting [1,17]. Finally, when  $z/\bar{x}$  is sufficiently larger than 1, above  $T_{\text{IMT}} = 357$  K, the system undergoes an insulator-metal transition (IMT) [9] with the four electrons per Ru arranged as shown in the M-long configuration reported in Fig. 1(c). IMT is accompanied by a crystallographic transition from a tetragonal (L- $Pbca$ , L stands for long  $c$ ) to an orthorhombic (S- $Pbca$ , S  $\rightarrow$  short  $c$ ) phase. This transition is so dramatic to break the crystals into pieces [15].

The strong link between conduction and structural properties [1,17] paves the way to control the electronic behavior by strain/epitaxial growth [18] or by inducing nonlinear phononic effects, for instance, through intense terahertz radiation [19–21]. Another relevant drive to induce the IMT is the electric field, despite that the structural changes indirectly induced in such a case are not yet clarified. Indeed, the electric field tuning of the conduction regime is of particular interest, since at room  $T$  the metallic state can be induced by a threshold field of about  $E_{\text{th}} \approx 50 \div 100$  V/cm [2,15,22], almost three orders of magnitude lower than in other Mott insulators [23]. This circumstance is very promising for possible applications in next-generation oxide electronics. As in other Mott materials [23,24], the IMT is accompanied by resistivity changes of several orders of magnitude [15]. As a first-order transition, IMT is generally unveiled by hysteretic electrical transport [15,25] for voltage drive [Fig. 1(b), blue dotted line]. Instead, voltage-current  $V - I$  characteristics with negative slope were reported for DC current drive, Fig. 1(c), red line [22,26].

However, one should be aware that different measurement protocols exist in the literature under the simple names of voltage or current drive. The difference in the procedures, on one hand, gives one perspective to look at an interesting system such as Ca-214, but also makes it difficult to compare the results obtained in different works. Recently, the

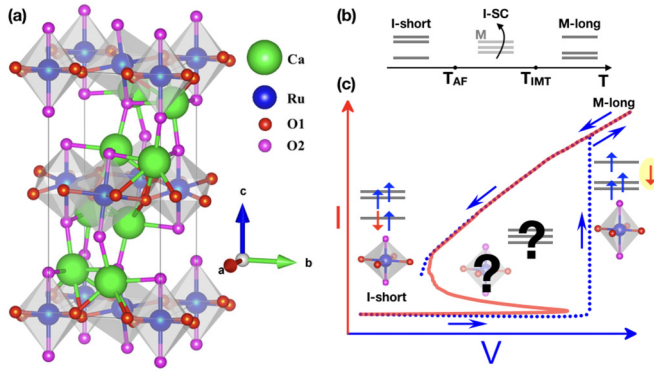


FIG. 1. (a) Crystallographic unit cell. (b) Sketch of the temperature evolution of the  $t_{2g}$  orbitals of Ru, see text for details. (c) Cartoon of the  $I - V$  curve: The hysteretic path for an electrical potential drive (blue) and the behavior for an electrical current drive (red) are shown. The characteristic octahedron shapes (the axes ratios are exaggerated for illustration purposes) and the levels'/electrons' characteristic arrangements are reported for the different regions of the  $I - V$  characteristic, corresponding to  $S\text{-}Pbca$  (I-short) and  $L\text{-}Pbca$  (M-long). The intermediate state with  $dI/dV < 0$  is the main objective of the paper.

investigation of nonequilibrium electronic and crystallographic phases emerging by current or voltage biasing the crystals has gained much attention. Indeed, a crystal structure supposing to be the manifestation of a semimetallic state was reported by a measurement protocol completely different from the one presented in this paper [27], while alternating insulating and metallic regions arranged in stripe patterns at the M-I phase boundary were observed in the regime of controlled constant current flow [26]. Moreover, it is now accepted that DC current biasing can be used to control the magnetic properties of the system, since, under current flow, strong diamagnetism is induced in pure Ca-214 and in  $\text{Ca}_3\text{Ru}_{1-x}\text{Ti}_x\text{O}_7$  [2,28] and AFM order is suppressed in pure Ca-214 [27,28].

In this paper, the electrical response of Ca-214 single crystals is investigated as a function of both  $T$  and the bias-current density,  $J$ , in the conduction regimes spanning from the insulating to the metastable (MS) state, precursor of the metallic one, where nonequilibrium processes possibly take place. In this way, the resistivity map,  $\rho(J, T)$ , of the system, where  $\rho$  is the electrical resistivity, is built. This study, systematically performed on a large number of crystals, is an extremely valuable starting point for further investigations, since it naturally highlights the different conducting regimes, as well as the characteristic temperatures and current densities, at which they set in. In particular, here the attention focuses on the less explored MS state, since poor information is currently available concerning both the conduction mechanisms and the corresponding crystallographic structure. For these reasons, the transport measurements are combined with x-ray diffraction (XRD) spectra acquired as a function of  $J$ , at room  $T$ .

## II. EXPERIMENTAL METHODS

High quality Ca-214 single crystals were grown by floating zone technique as described in Ref. [29]. The typical average

dimensions of the analyzed crystals are about  $(2.0 \times 1.0 \times 0.150) \text{ mm}^3$ . Great care was paid to the reproducibility of the presented results. To this purpose, a big amount of data was collected on several Ca-214 single crystals, which all behaved consistently. This assures the reliability of the presented measurements.

The phase diagram of Ca-214 is very rich as well as being quite far from being fully explored and understood. For this reason, an extremely precise control of the actual state of the sample, as a function of the external conditions, is required to efficiently study this system. Moreover, an absolutely methodical approach is essential to obtain reproducible and scientifically sound results. In this respect, it is necessary to clarify that many different measurement protocols exist in the literature under the simple names of current or voltage drive. For a system such as Ca-214, with unconventional and very slow responses to electric drive, this leads to the great opportunity of having many different and interesting perspectives that all contribute to the overall understanding of the complex physics of this material.

On the other hand, the comparison of the results obtained by different experimental procedures may not be easy. Here, a very straightforward measurement protocol was used, namely the sample was current biased in a continuous mode, with the use of a steady current source. This approach can give access to different states of the system compared with those already reported in the literature. For instance, in the work of Bertinshaw *et al.*, the authors first use the voltage to bias the sample, and once the switching to the metallic phase is achieved, let an electrical current to flow in the system [27]. Instead, in Ref. [26], voltage and current are simultaneously controlled by the use of two variable resistors.

Here, electrical transport measurements, both resistivity versus temperature, for different values of the bias current, and  $V - I$  characteristics as a function of  $T$ , were performed with a two-probe method by current biasing the crystals along the  $c$  direction with a Keithley 2635 SourceMeter and reading the voltage drop with a Keithley 2182A Nanovoltmeter. Due to the high resistance values of the crystals compared to the ones of the wiring and the contacts, this method does not affect the measurement accuracy [2,15,28]. The electrical current was chosen as the biasing stimulus since it is capable of driving the system into an intermediate state which, as demonstrated, does not have an equilibrium analog and strongly differs from the insulating or the metallic thermodynamic phases explored by the voltage-driven measurement. The accessible area of the resistivity map is determined by the limit of the SourceMeter, which was set at 200 V.

Extreme attention was paid to adopt all the precaution necessary to maximize sample cooling as well as to reduce contact resistance at the sample ends. First, to keep contact resistance as low as possible, silver pads were sputtered on the crystal faces from which gold wires (diameter  $25 \mu\text{m}$ ) were connected by an epoxy silver-based glue with the external wiring. Then, to achieve a fair temperature control, the thermal coupling between the sample and the Cernox thermometer was carefully implemented: The crystals were thermally anchored with a small amount of cryogenic high vacuum grease on a custom-built dip probe on the massive high-thermal-conductivity copper sample holder in which the

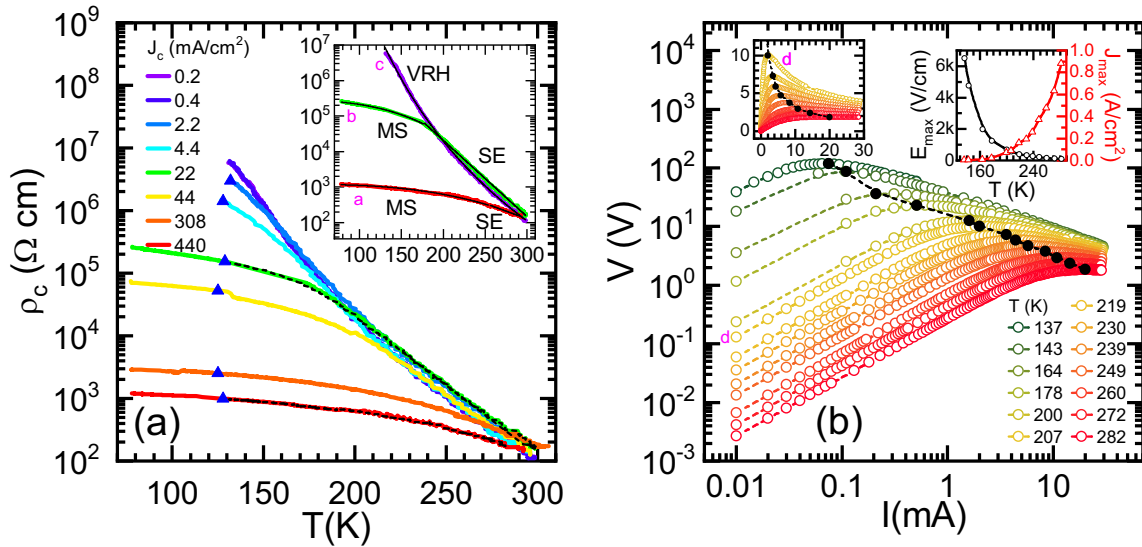


FIG. 2. (a) Resistivity versus temperature of Ca-214 single crystal. The  $\rho(T)$  curves for  $J = 22$  (green) and  $440$  (red)  $\text{mA}/\text{cm}^2$  measured by first decreasing  $T$  (continuous lines) and then heating the sample (dashed lines) are highlighted. The blue triangles indicate when the irreversibility described in the text sets in. Inset: Selection of  $\rho(T)$  curves (labeled as a, b, c) plotted together with the fits corresponding to different conduction regimes (VRH, SE, and MS). (b)  $V - I$  characteristics as a function of  $T$  on a double logarithmic scale. A representative curve is labeled by the letter d. The black solid circles connect the maximum of all the curves,  $(V_{\max}, I_{\max})$ , as better shown on linear scales (left inset). Right inset: Temperature dependence of  $E_{\max}$  (left scale) and  $J_{\max}$  (right scale).

thermometer was embedded, in close contact with the crystal. The temperature was changed by lowering the probe into a cryogenic liquid nitrogen storage dewar by taking advantage of the temperature stratification naturally occurring in the vapor space above the liquid surface. The thermal stability is guaranteed by the proper design of the copper sample holder and by the extremely slow temperature sweeps.

X-ray diffraction measurements in a specular  $\omega$ - $2\theta$  geometry ( $\omega$  is the radiation incident angle on the sample surface, while  $2\theta$  is the angle between the incident and the diffracted beam) were performed by using a Philips X'Pert-MRD high-resolution analytic diffractometer equipped with a four-circle cradle. A Cu  $K_{\alpha 1}$  ( $\lambda = 1.5406 \text{ \AA}$ ) source was used at  $40 \text{ kV}$  and  $40 \text{ mA}$ . Measurements were carried out by using monochromatic radiation obtained by equipping the diffractometer with a four-crystal Ge 220 Bartels asymmetric monochromator and a graded parabolic Guttman mirror positioned on the primary arm. On the secondary arm, the diffracted beam reaches the detector with an angular divergence of  $12 \text{ arcsec}$  crossing a triple axis attachment and undergoing three (002) reflections within a channel-cut Ge Crystal.

### III. RESULTS

#### A. Electrical transport measurements

The temperature dependence of the resistivity measured along the  $c$  axis for selected values of  $J$  is reported in semilogarithmic scale in Fig. 2(a). It is important to notice that analogous results were obtained on all the investigated samples. By increasing  $J$ ,  $\rho$  is lowered of up to four orders of magnitude [2,22]. Moreover, despite  $\rho$  always being a decreasing function of the temperature ( $d\rho/dT < 0$ ) [10], the shape of the resistivity curves evolves as  $J$  is increased and

distinct  $\rho(T)$  behaviors can be observed, as indicated in the inset of Fig. 2(a) by the labels VRH, SE, and MS, which stand for variable range hopping, semiconducting, and metastable, respectively, as discussed more in detail in the following. In addition, a critical value  $J^{\text{sep}} \approx 0.4 \text{ mA}/\text{cm}^2$  can be identified, which sets the change in the concavity of the  $\rho(T)$  curves in semilogarithmic scale, in accordance with Ref. [2]. The curves measured for  $J < J^{\text{sep}}$  hardly depend on the value of  $J$ , as in the case of the ones for  $J = 0.2$  and  $0.4 \text{ mA}/\text{cm}^2$ , which completely overlap [22]. By measuring  $\rho$ , both lowering and increasing  $T$ , an irreversible behavior, never reported in the literature, was observed. Indeed, there are portions of the  $\rho(T)$  curves whose accessibility depends on the sample history, as shown, for example, for  $J = 22$  and  $440 \text{ mA}/\text{cm}^2$ . Here the continuous lines indicate the data obtained by lowering  $T$ . For  $J < J^{\text{sep}}$ , the resistance surge beyond the measurable range of the voltmeter at a characteristic temperature,  $T^{\text{irr}} \approx 130 \text{ K}$ , while for  $J > J^{\text{sep}}$  the resistance is still measurable below this value. However, by increasing the temperature from the lowest  $T$  reached in the experiment, a measurable  $\rho$  is detected only for  $T > T^{\text{irr}}$  (black dotted lines). The values of  $T^{\text{irr}}$  are represented as blue triangles in the figure. Interestingly, for all the analyzed crystals and independently on  $J$ ,  $T^{\text{irr}} \approx 130 \text{ K}$ , a value comparable with  $T_{\text{AFM}}$ . Contrary to what reported in the literature, the measure of  $\rho(T)$  can give indications of the magnetic ordering temperature in Ca-214 [10]. Moreover, this result confirms that  $J$  induces a more conductive MS state where AFM is suppressed [27] and, more generally, that  $J$  can be used to control the magnetic ordering of this class of materials [2,27,28]. A more detailed analysis of this result is beyond the scope of this paper and will be subject of future studies.

In Fig. 2(b), a selection of  $V - I$  characteristics as a function of  $T$  obtained by  $I$  biasing the sample along the  $c$



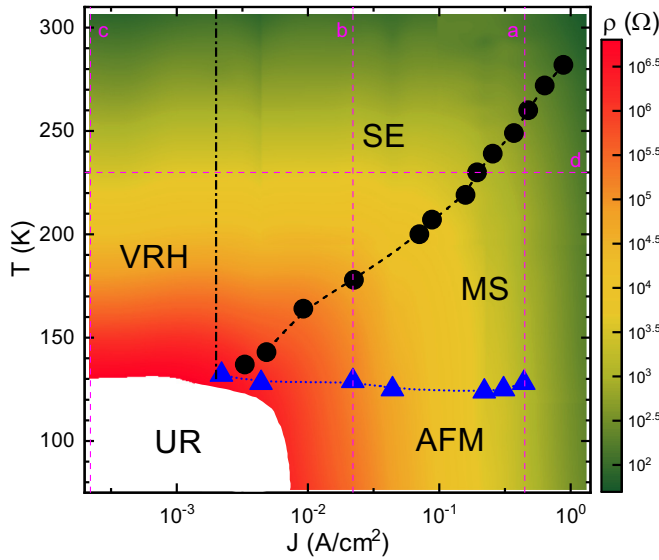


FIG. 3.  $\rho(J, T)$  contour plot of the crystal resistivity obtained by combining the  $\rho(T)$  and the  $V - I$  curves. The  $\rho(T)$  [ $(V - I)$ ] curves labeled by the letters a, b, and c (d) in Fig. 2(a) [2(b)] are reported here. The different regions corresponding to different conducting regimes (UR, VRH, SE, MS, and AFM) are highlighted. The blue triangles (black circles) are the same as Fig. 2(a) [2(b)].

axis is shown on a double logarithmic scale. Beyond the low  $J$  regime, when the samples show a clear insulating behavior, a negative differential resistance is observed [26,30], in accordance with the dramatic reduction of resistivity observed in the  $\rho(T)$  curves by increasing  $J$ . By further increasing the current, an ohmic dependence, signature of the IMT, is expected [15]. However, this threshold was not exceeded to preserve the crystal integrity and measure the whole resistivity map on the same sample. The change in the conduction results in a maximum in the characteristics at  $(V_{\max}, I_{\max})$  [or equivalently at  $(E_{\max}, J_{\max})$ ], as highlighted in Fig. 2(b) by black circles, both in the main panel and in the inset on the left, where the shape of the curves on a linear scale can be better appreciated. At room temperature,  $E_{\max} \approx 100$  V/cm and  $J_{\max} \approx 0.9$  A/cm². Their temperature dependence is reported in the right inset of Fig. 2(b). While  $E_{\max}$  (black points, left scale) increases with  $T$  [15],  $J_{\max}$  (red points, right scale) decreases on cooling. This latter behavior is counterintuitive and requires further analysis to be understood. It is worth noting that  $E_{\max}$  should not be confused with  $E_{\text{th}}$ .  $E_{\text{th}}$  is the value at which, driving with electrical potential, one reaches the thermodynamic metallic phase (M-long) [15], while  $E_{\max}$  is the value at which, driving with  $J$ , one reaches the MS state.

By combining both  $\rho(T)$  curves measured for different values of  $J$  and  $V - I$  characteristics as a function of  $T$ , it is possible to draw the  $\rho(J, T)$  contour plot of the crystal resistivity shown in Fig. 3. For the sake of clarity, only a selection of  $\rho(T)$  curves, representative of different conduction behaviors, are reported in the Fig. 3 as vertical lines (a, b, c), while the same  $V - I$  curve labeled as d in Fig. 2(b) is represented as a horizontal line (see Fig. 3). The resulting  $\rho(J, T)$  phase diagram comprises different regions, corresponding to different conducting regimes (UR, VRH, SE, MS, and AFM),

as marked by the three contours present in the Fig. 3. The dot-dashed vertical line represents the value of  $J^{\text{sep}}$ . The positions of the maximum of the  $V - I$  curves at the investigated temperature are represented by black dashes [as in Fig. 2(b)]. Finally, the blue dotted line at  $T^{\text{irr}} \approx 130$  K indicates the nonreversible behavior of the  $\rho(T)$  curves, namely, the onset of the AFM ordering.

Accordingly, the following conducting regimes are identified. First, in the limit of both low  $J$  and  $T$ , there is the so-called unexplored region (UR), namely, a deeply insulating region which is not accessible due to the limit of the experimental setup used. Then, by moving along the  $J$  axis ( $J < J^{\text{sep}}$ , all  $T$ ), the  $\rho(T)$  has a variable range hopping behavior with a power coefficient of about 0.25, typical of 3D systems (for all the details about the fitting of the  $\rho(T)$  curves, the reader can refer to the Appendices). Here the resistivity is not affected by the bias current density. For  $J > J^{\text{sep}}$ , namely, by crossing the dot-dashed line, a reduction of  $\rho$  is observed [22]. From this side, regions SE and MS, divided by the black dashed line, identify, respectively, the semiconducting and the MS regimes. In region SE ( $J_{\max} > J > J^{\text{sep}}$ ,  $T > T_{\max}$ ), the best  $\rho(T)$  fit is obtained by using a decreasing (negative) exponential behavior resembling that of an intrinsic semiconductor at sufficiently high  $T$ , that is, a shallow insulator whose gap is comparable to the temperature range under analysis. In region MS ( $J > J_{\max}$ ,  $T < T_{\max}$ ), the  $\rho(T)$  has a behavior that is very different from both that of an insulator (decreasing, positive concavity in both linear and log scale) and of a metal (increasing, positive concavity in both linear and log scale), but a decreasing behavior with negative (positive) concavity in log (normal) scale is measured. Indeed, this change of concavity in the log scale allows us to identify  $J^{\text{sep}}$ . Such a situation, still interpreted in the VRH paradigm, marks the divergency of the localization length. This can be interpreted as the signal that at least a portion of the system becomes conducting, leading to a resistivity that strongly resembles those of alloys and whose best fit is obtained with a decreasing (negative) exponential with a power coefficient of about 3. The exact type of conducting mechanism remains to be further investigated in this case. The intrinsic dependence on time of the process makes it difficult to characterize through instruments, and related concepts, that are meant to work at equilibrium.

## B. X-ray diffraction measurements

XRD measurements were performed at room  $T$  by current biasing the crystal to complement the electronic characterization and gain access to the microscopic properties of the different conducting regimes. In Fig. 4(a), the dependence of the  $c$ -lattice parameter (left scale) on the normalized current density,  $J/J_{\max}$ , is superimposed to the normalized  $E - J$  characteristic (right scale), to allow the comparison among different samples; characteristic level arrangements (I-SC, M', M-long, see below) are also reported. The values of  $c$  were calculated according to the Bragg law by following the position of the (006) reflection of the XRD  $\omega$ - $2\theta$  scans. The values of the  $c$  axis plotted by black-closed circles represent the elongation of the short  $c$  axis of the insulating S phase at  $J = 0$  ( $c = 11.914$  Å, magenta closed circle) [15]. This

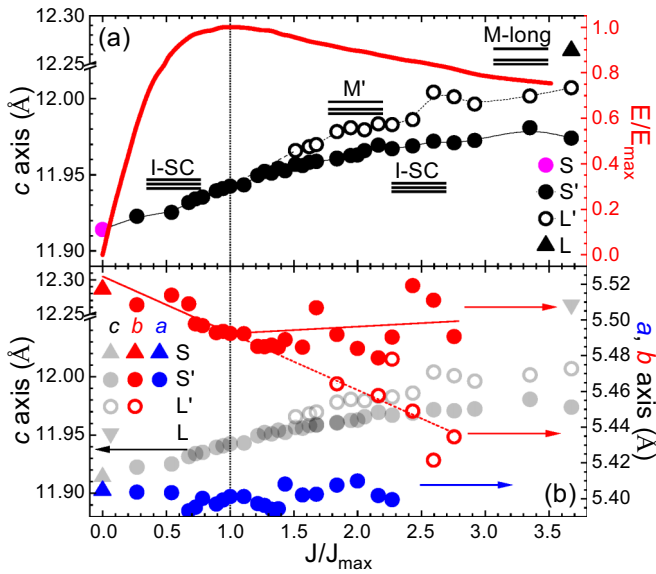


FIG. 4. (a) Left scale: Dependence of the  $c$ -lattice parameter corresponding to the different crystallographic phases (S, S', L', and L) as a function of  $J/J_{\max}$ . Right scale: Normalized  $V-I$  curve,  $E/E_{\max} - J/J_{\max}$ , measured on the same crystal. Characteristic level arrangements (I-SC, M', M-long) are also reported. (b) On the left (right) scale, the dependence of the  $c$ - ( $a$ -,  $b$ -) lattice parameter as a function of  $J/J_{\max}$  is plotted. The error bars are smaller than the data symbols. Lines are guides to eye.

change produces a distortion of the lattice cell, which now is labeled S'. Interestingly, at  $J \approx J_{\max}$ , a new phase indicated as L', and represented by open circles, clearly emerges. The  $c$  axis of L' also elongates by increasing  $J$  and is well detected in the whole investigated current range, which covers the region of negative differential resistance of the  $E-J$  curve. Finally, at  $J/J_{\max} \approx 3.7$ , the diffraction peak associated with the metallic L phase appears ( $c = 12.264$  Å, black triangle) [15].

These measurements demonstrate that in the MS state, a new, possibly metallic (L'), crystallographic phase coexists with the short insulating one (S') in quite a wide range of current values and even with the metallic one (L), at the maximum current reached in the experiment. In Fig. 4(b), the dependence on  $J/J_{\max}$  of the lattice parameters  $a$  and  $b$ , calculated from the position of the reflections (208) and (028), respectively, is compared with the  $c$  axis. Noticeably, while the value of the  $a$  axis is almost constant, the  $b$  axis (red dots) splits in two branches at  $J/J_{\max} \approx 1$  as the  $c$  axis does. In the same region, corresponding to the appearance of the L' phase, statistical scattering is present in the  $b$ -axis data. This can be interpreted as due to the release of the in-plane strain while trying to accommodate both phases (S' and L') in the crystal. From a careful inspection of the data, it also emerges that the statistical scattering of the two phases is overall complementary. It is worth noting that the L' phase moves toward a metallic tetragonal structure, while the S' phase slowly relaxes back toward the S one (in terms of crystallographic axis). Indeed, once the L' phase nucleates and develops, S will sustain only a smaller fraction of the flowing current. It is worth noticing that the values of the lattice parameters, both in the S and in the L phases, are consistent with the

results reported in the literature [15,16,31]. In particular, the value of the  $c$  axis in the metallic phase (L) is in accordance with the ones reported for structural transitions induced by electric field, pressure, and temperature [15]. This indicates that, contrary to the MS state, L is a real thermodynamic phase.

#### IV. DISCUSSION

The emergence of a metallic phase (L') in the system would explain both the puzzling negative differential resistivity of the MS regime and the counterintuitive increase of  $J_{\max}$  with  $T$ . In fact, to sustain a systematic increase of current flow in an overall insulating state, at a certain critical current density, dependent on temperature, and comparable with  $J_{\max}(T)$ , the system finds it energetically more convenient to nucleate a more conductive crystallographic phase, L'. Consequently, above  $J_{\max}(T)$ , the electrical potential needed to further increase the current flow reduces, while the more-conductive L' phase grows. On increasing  $T$ , the S' phase itself can sustain more current, since it becomes less insulating. Accordingly,  $J_{\max}(T)$  is an increasing function of  $T$ . This is just one of the clearest signatures that the emergence of L' is not a classical effect driven by Joule heating, but that it comes from a much more subtle and complex energy balance.

The remarkable increase of  $c$  and decrease of  $b$  in the L' phase is definitely compatible with a significant decrease of the ratio  $\bar{x}/z$  that would steadily lead to a metallic behavior of that portion of the material. To check this hypothesis, a transformation matrix computed in Ref. [32] by means of DFT + U calculations was used. This allows one to track the effect of applied strain on  $a$ ,  $b$ , and  $c$  and, in particular, as this reflects on  $x$ ,  $y$ , and  $z$  (see Appendices). The obtained related changes of  $x$ ,  $y$ , and  $z$  give, as expected, a decreasing ratio of  $\bar{x}/z$ , following the evolution with increasing current from

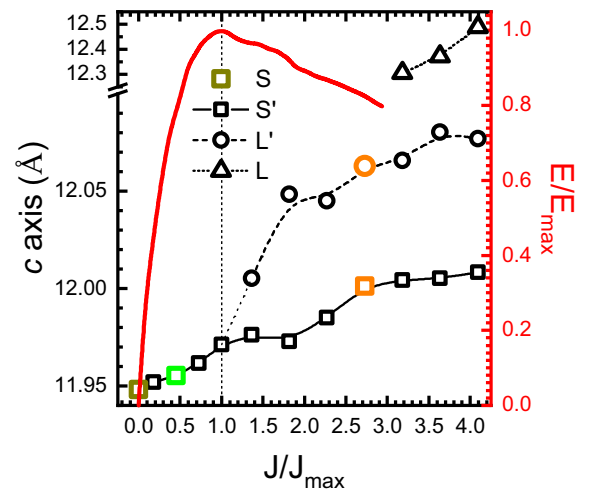


FIG. 5. Left scale: Dependence of the  $c$ -lattice parameter corresponding to the different crystallographic phases (S, S', L', and L) at room temperature as a function of the normalized bias current density  $J/J_{\max}$ . The bigger colored points indicate the values of the  $c$  axis extracted from the XRD scans of the corresponding color reported in Fig. 2. Right scale: Normalized  $V-I$  curve,  $E/E_{\max} - J/J_{\max}$ , measured at room temperature on the same crystal.

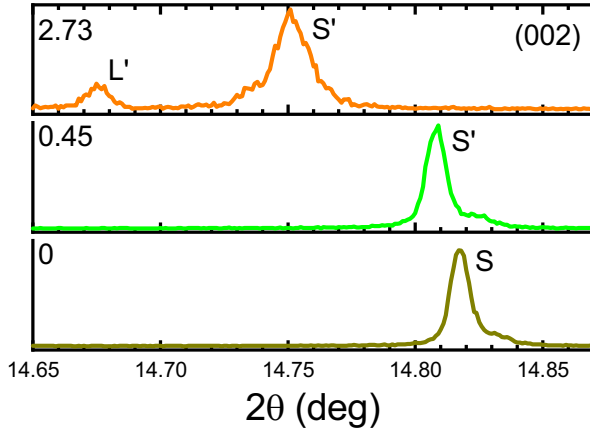


FIG. 6. Representative  $\omega$ - $2\theta$  scans of the (002) reflections are reported for different values of the normalized bias current  $J/J_{\max}$  for the same crystal of Fig. 5. The labels on the diffraction peaks correspond to the different crystallographic phases (S, S', L') present in the different conduction regimes.

S' to L', but also two unpredictable results: first, above  $J_{\max}$ , that is, once L' sets in, S' goes back toward the values of  $x$ ,  $y$ , and  $z$  characteristics of S; second, the decrease of  $\bar{x}/z$  is mainly determined by the decrease of  $x$  and not by the increase of  $z$ . Once the system has the possibility to fully exploit the L' phase to allow an increasingly current flow, S' phase can relax back to the S one. The complicated intertwining of rotation, tilt, and distortion maps the increase of  $c$  mainly on a reduction of  $\bar{x}$  than on an increase of  $z$ .

## V. CONCLUSIONS

In summary, DC current drive was used to determine the  $\rho(J, T)$  phase diagram. By taking advantage of this protocol, it was possible to access a region of the phase diagram not yet explored and to unveil the nucleation and evolution of a metallic crystallographic phase, L', completely compatible with the transport data. Its corresponding cell dimensions depart from those of the insulating *short* phase and approach

those of the metallic *long* phase. The main octahedral axis and the corresponding Ru levels of this phase were theoretically obtained: the phase L' is more conducting than S' and can be considered a precursor of the metallic L phase.

These results explain the unexpected and counterintuitive results of the transport data and completely determine the behavior in the MS phase. Such findings are consistent with the literature, and represent a significant improvement of the current comprehension of a complex system such as Ca-214, opening perspectives in its microscopic characterization. For instance, spectroscopic measurements under electrical current drive may represent a valuable validation of the present findings.

## ACKNOWLEDGMENTS

The authors gratefully acknowledge Y. Maeno and G. Mattoni for useful discussions and I. Nunziata for technical support.

## APPENDIX A: XRD DATA SUPPLEMENT

To provide further evidence of the coexistence of the three distinct crystallographic phases in the current-induced MS state, additional XRD data for another single crystal are presented in Fig. 5. Here the values of the  $c$ -lattice parameters as a function of the normalized electrical current density were derived from the (002) reflection. Again the comparison with the normalized  $E - J$  curve measured for the same crystal (right scale) confirms that the S' phase splits into the L' phase at  $J \approx J_{\max} = 0.8 \text{ A/cm}^2$  (see vertical dashed line). This phase is well distinguished in all the investigated current ranges from the other two diffraction peaks, as shown in Fig. 6, where three representative  $\omega$ - $2\theta$  scans of the (002) reflection are reported for different values of  $J/J_{\max}$ , corresponding to different regions of the  $E/E_{\max} - J/J_{\max}$  characteristic. It is evident that before reaching the maximum of the  $E/E_{\max} - J/J_{\max}$  characteristic, namely, in the insulating regime, only the peaks identifying the phases S and S' are present (dark yellow and green scans, respectively). Above  $J_{\max}$ , the diffraction peak of

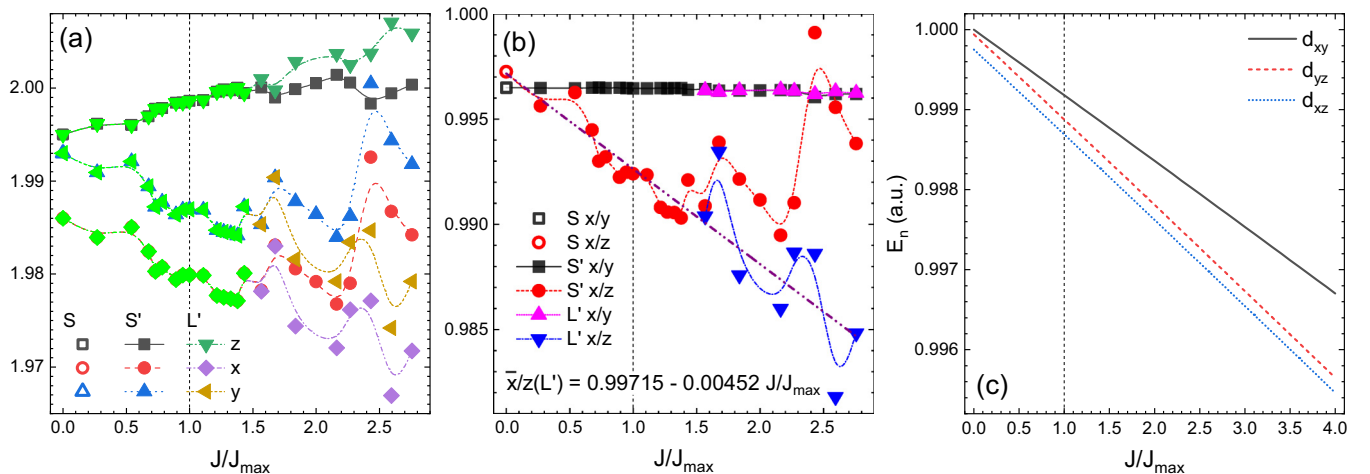
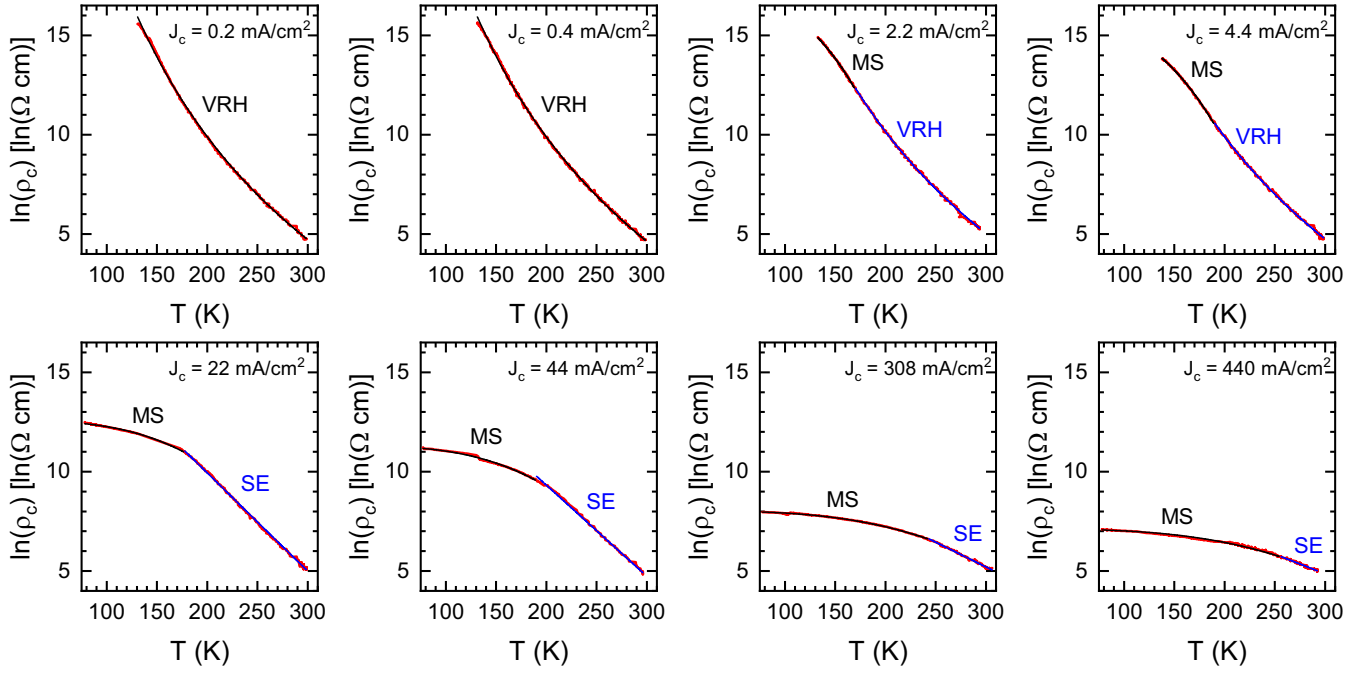


FIG. 7.  $x$ ,  $y$ , and  $z$  (a) and  $x/y$  and  $\bar{x}/z$  (b) as functions of  $J/J_{\max}$  for phases S, S', and L'. (c) Energies (in arbitrary units) of the Ru  $d_{xy}$ ,  $d_{yz}$ , and  $d_{xz}$   $\text{RuO}_6$  octahedra levels as functions of  $J/J_{\max}$  for L' phase (S' phase for  $J \leq J_{\max}$ ).

FIG. 8. Least-squares fits of  $\ln(\rho_c)$  as a function of  $T$  for various values of  $J_c$ .

the L' phase develops, as shown by the orange line, acquired at  $J/J_{\max} = 2.73$ .

## APPENDIX B: THEORETICAL METHODS

### 1. RuO<sub>6</sub> octahedra

#### a. Crystal field

The RuO<sub>6</sub> complex is an octahedron whose vertices are occupied by 6 O atoms and its center by a Ru atom. Such a type of Ru-O coordination, according to the Jahn-Teller effect [33], splits the  $d$  levels of the Ru in two groups:  $e_g$ ,  $d_{x^2-y^2}$  and  $d_{3z^2-r^2}$ , and  $t_{2g}$ ,  $d_{xy}$ ,  $d_{yz}$  and  $d_{xz}$ . In the first group,  $e_g$ , the orbitals have lobes pointing directly toward the directional  $p$  orbitals of O and therefore lie higher in energy. On the other hand, in the second group,  $t_{2g}$ , the actual distances of the apical oxygens Ru-O2,  $z$  in the main text, and of the in-plane oxygens Ru-O1,  $x$  and  $y$  in the main text (and  $\bar{x}$  their average), determine the degree of degeneracy of the three levels: A perfect octahedron ( $z = x = y$ ) leads to three perfectly degenerate levels. Instead, the smaller  $x$  is with respect to  $y$  (at fixed  $z$ ), the higher in energy lies the level  $d_{xz}$  with respect to  $d_{yz}$ ; as well as the smaller  $\bar{x}$  is with respect to  $z$ , the higher in energy lies the level  $d_{xy}$  with respect to the  $d_{yz}$ - $d_{xz}$  doublet.

As schematically reported in Fig. 1(b) in the main text, the order in energy of the  $t_{2g}$  levels is fundamental to establish how the four electrons per Ru present in the system decide to occupy such levels. As a consequence, this determines the transport properties of the related state. In the I-short state,  $z/\bar{x} < 1$  and  $d_{xy}$  is lower in energy with respect to the  $d_{yz}$ - $d_{xz}$  doublet with a crystal field gap that can be so large that the electrons prefer to arrange in pairs in  $d_{xy}$  level although the local Coulomb repulsion would avoid that. The remaining two electrons can accommodate the  $d_{yz}$ - $d_{xz}$  doublet according

to the Hund's rule with parallel spins and such a configuration, at low enough temperatures, leads to an insulating antiferromagnetic state. At higher temperatures, since  $z/\bar{x}$  gets closer and closer to 1, the levels become almost degenerate. In this situation, the strong correlations prevent the system from behaving as a metal, but still as an insulator, by splitting the  $d_{yz}$  and  $d_{xz}$  levels in lower and upper Mott-Hubbard bands. By further increasing the temperatures,  $z/\bar{x}$  become sufficiently larger than 1 to have the  $d_{yz}$ - $d_{xz}$  doublet below the  $d_{xy}$  level and lead to a metal. In this case, three electrons fill in the levels according to the Hund's rule and one electron gets free to move in the lattice.

#### b. Crystallographic axes versus RuO distances

By means of DFT + U calculations, Han and Millis [32] found a transformation matrix relating the variations of the crystallographic axis  $\delta a$ ,  $\delta b$ , and  $\delta c$  to the variations of the Ru-O distances in the RuO<sub>6</sub> octahedra, that is,  $\delta x$ ,  $\delta y$ , and  $\delta z$ :

$$\begin{pmatrix} \delta x^+ \\ \delta z \\ \delta x^- \end{pmatrix} = \begin{pmatrix} 0.3740 & -0.0053 & -0.0698 \\ -0.0517 & 0.0746 & 0.0313 \\ -0.0082 & -0.0059 & -0.0015 \end{pmatrix} \begin{pmatrix} \delta a^+ \\ \delta c \\ \delta a^- \end{pmatrix}, \quad (\text{B1})$$

where  $\delta x^\pm = \frac{1}{\sqrt{2}}(x \pm y)$ , and  $\delta a^\pm = \frac{1}{\sqrt{2}}(a \pm b)$ . This matrix allows one to find the values of  $x$ ,  $y$ , and  $z$  given those of

TABLE I. Variable-range hopping regime fitting parameters.

$J$ (mA/cm <sup>2</sup> )	$T$ (K)	$A$	$B$	$C$
0.2	All	-43.9	202.2	-0.25
0.4	All	-44.6	205.1	-0.25
2.2	>170	-43.0	199.7	-0.25
4.4	>190	-43.5	200.7	-0.25



TABLE II. Metastable regime fitting parameters.

$J$ (mA/cm <sup>2</sup> )	$T$ (K)	$A$	$B$	$C$	$T_0$ (K)
2.2	<170	17.2	$-1.01 \times 10^{-6}$	3	99.6
4.4	<190	15.9	$-7.89 \times 10^{-7}$	3	108
22	<177	12.5	$-2.82 \times 10^{-7}$	3	152
44	<189	11.3	$-2.53 \times 10^{-7}$	3	158
308	<243	8.01	$-9.84 \times 10^{-8}$	3	217
440	<256	7.10	$-8.31 \times 10^{-8}$	3	229

$a$ ,  $b$ , and  $c$  for the two phases, S' and L', emerging from the S one on applying an electrical current drive [see Fig. 7(a)]. It was then possible to obtain the two fundamental ratios  $x/y$  and  $\bar{x}/z$  in the S' and L' phases [see Fig. 7(b)]. A least-squares linear fit of the ratio  $\bar{x}/z$  for the L' phase (following the one of the S' phase for  $J \leq J_{\max}$ ) gave very accurate results and the related fit parameters are reported directly in the figure [see Fig. 7(b)]. Given the almost constant ratio  $x/y$  and the linear fit of the ratio  $\bar{x}/z$ , it has been possible to compute the relative energies of the  $d_{xy}$ ,  $d_{yz}$ , and  $d_{xz}$  levels [see Fig. 7(c)]. This supports our interpretation that the unconventional and puzzling behavior of the MS state is due to the emergence of the metallic phase L' in the system.

## 2. Conductive regimes: VRH, SE, and MS

All the curves reporting the behavior of the resistivity  $\rho$  as a function of the temperature  $T$ , for different values of  $J$ , have been least-squares fitted with the same generic allometric function (see Fig. 8):

$$\ln(\rho) = A + BT^C. \quad (\text{B2})$$

TABLE III. Semiconductor regime fitting parameters.

$J$ (mA/cm <sup>2</sup> )	$T$ (K)	$A$	$B$	$C$	$T_0$ (K)
22	>177	19.8	-0.0494	1	20.2
44	>189	18.5	-0.0458	1	21.8
308	>243	12.7	-0.0249	1	40.2
440	>256	10.8	-0.0197	1	50.8

According to the sign of  $B$  and the value of  $C$ , it is possible to identify three distinct conducting regimes (VHR, SE, and MS) which set in a specific range of temperatures, depending on the value  $J$  (see Tables I–III). The values of  $C$  have been chosen according to the closest value for all currents and temperatures in the regime to avoid excessive fluctuations in the other parameters.

It is worth noting that such unbiased fits of the  $R(T)$  curves independently and accurately reproduce the position of the maximum in the I–V characteristics.

### a. Variable range hopping (VRH)

In this case, it is  $B > 0$  and  $C < 0$ . The results of the fitting procedure reported in Table I are compatible with a 3D system.

### b. Metastable (MS)

In this case, it is  $B < 0$  and  $C > 0$ . In Table II, the fitting parameters corresponding to the MS regime are reported.  $T_0 = |B|^{-\frac{1}{C}}$  is the equivalent activation temperature.

### c. Semiconductor (SE)

In this case, it is  $B < 0$  and  $C = 1$ . The fitting procedure returns the values reported in Table III.  $T_0 = |B|^{-1}$  is the activation temperature.

- [1] E. Gorelov, M. Karolak, T. O. Wehling, F. Lechermann, A. I. Lichtenstein, and E. Pavarini, *Phys. Rev. Lett.* **104**, 226401 (2010).
- [2] C. Sow, S. Yonezawa, S. Kitamura, T. Oka, K. Kuroki, F. Nakamura, and Y. Maeno, *Science* **358**, 1084 (2017).
- [3] S. Riccò, M. Kim, A. Tamai, S. McKeown Walker, F. Y. Bruno, I. Cucchi, E. Cappelli, C. Besnard, T. K. Kim, P. Dudin, M. Hoesch, M. J. Gutmann, A. Georges, R. S. Perry, and F. Baumberger, *Nat. Commun.* **9**, 4535 (2018).
- [4] L. Das, F. Forte, R. Fittipaldi, C. G. Fatuzzo, V. Granata, O. Ivashko, M. Horio, F. Schindler, M. Dantz, Y. Tseng, D. E. McNally, H. M. Rønnow, W. Wan, N. B. Christensen, J. Pellicciari, P. Olalde-Velasco, N. Kikugawa, T. Neupert, A. Vecchione, T. Schmitt, M. Cuoco, and J. Chang, *Phys. Rev. X* **8**, 011048 (2018).
- [5] D. G. Porter, V. Granata, F. Forte, S. Di Matteo, M. Cuoco, R. Fittipaldi, A. Vecchione, and A. Bombardi, *Phys. Rev. B* **98**, 125142 (2018).
- [6] P. Steffens, O. Friedt, P. Alireza, W. G. Marshall, W. Schmidt, F. Nakamura, S. Nakatsuji, Y. Maeno, R. Lengsdorf, M. M. Abdelmeguid, and M. Braden, *Phys. Rev. B* **72**, 094104 (2005).
- [7] T. Mizokawa, L. H. Tjeng, G. A. Sawatzky, G. Ghiringhelli, O. Tjernberg, N. B. Brookes, H. Fukazawa, S. Nakatsuji, and Y. Maeno, *Phys. Rev. Lett.* **87**, 077202 (2001).
- [8] D. Sutter, C. G. Fatuzzo, S. Moser, M. Kim, R. Fittipaldi, A. Vecchione, V. Granata, Y. Sassa, F. Cossalter, G. Gatti, M. Grioni, H. M. Rønnow, N. C. Plumb, C. E. Matt, M. Shi, M. Hoesch, T. K. Kim, T.-R. Chang, H.-T. Jeng, C. Jozwiak, A. Bostwick, E. Rotenberg, A. Georges, T. Neupert, and J. Chang, *Nat. Commun.* **8**, 15176 (2017).
- [9] S. Nakatsuji and Y. Maeno, *J. Solid State Chem.* **156**, 26 (2001).
- [10] G. Cao, S. McCall, M. Shepard, J. E. Crow, and R. P. Guertin, *Phys. Rev. B* **56**, R2916 (1997).
- [11] F. Nakamura, *J. Phys. Soc. Jpn.* **76**, 96 (2007).
- [12] P. L. Alireza, F. Nakamura, S. K. Goh, Y. Maeno, S. Nakatsuji, Y. T. C. Ko, M. Sutherland, S. Julian, and G. G. Lonzarich, *J. Phys.: Condens. Matter* **22**, 052202 (2010).
- [13] J. P. Carlo, T. Goko, I. M. Gat-Malureanu, P. L. Russo, A. T. Savici, A. A. Aczel, G. J. MacDougall, J. A. Rodriguez, T. J. Williams, G. M. Luke, C. R. Wiebe, Y. Yoshida, S. Nakatsuji, Y. Maeno, T. Taniguchi, and Y. J. Uemura, *Nat. Mater.* **11**, 323 (2012).



- [14] D. Sutter, M. Kim, C. E. Matt, M. Horio, R. Fittipaldi, A. Vecchione, V. Granata, K. Hauser, Y. Sassa, G. Gatti, M. Grioni, M. Hoesch, T. K. Kim, E. Rienks, N. C. Plumb, M. Shi, T. Neupert, A. Georges, and J. Chang, *Phys. Rev. B* **99**, 121115(R) (2019).
- [15] F. Nakamura, M. Sakaki, Y. Yamanaka, S. Tamaru, T. Suzuki, and Y. Maeno, *Sci. Rep.* **3**, 2536 (2013).
- [16] M. Braden, G. André, S. Nakatsuji, and Y. Maeno, *Phys. Rev. B* **58**, 847 (1998).
- [17] G. Zhang and E. Pavarini, *Phys. Rev. B* **95**, 075145 (2017).
- [18] T. Kikuzuki and M. Lippmaa, *Appl. Phys. Lett.* **96**, 132107 (2010).
- [19] M. Rini, R. Tobey, N. Dean, J. Itatani, Y. Tomioka, Y. Tokura, R. W. Schoenlein, and A. Cavalleri, *Nature* **449**, 72 (2007).
- [20] H. Ehrke, R. I. Tobey, S. Wall, S. A. Cavill, M. Först, V. Khanna, T. Garl, N. Stojanovic, D. Prabhakaran, A. T. Boothroyd, M. Gensch, A. Mirone, P. Reutler, A. Revcolevschi, S. S. Dhesi, and A. Cavalleri, *Phys. Rev. Lett.* **106**, 217401 (2011).
- [21] H. Ichikawa, S. Nozawa, T. Sato, A. Tomita, K. Ichiyanagi, M. Chollet, L. Guerin, N. Dean, A. Cavalleri, S.-i. Adachi, T.-h. Arima, H. Sawa, Y. Ogimoto, M. Nakamura, R. Tamaki, K. Miyano, and S.-y. Koshihara, *Nat. Mater.* **10**, 101 (2011).
- [22] R. Okazaki, Y. Nishina, Y. Yasui, F. Nakamura, T. Suzuki, and I. Terasaki, *J. Phys. Soc. Jpn.* **82**, 103702 (2013).
- [23] E. Janod, J. Tranchant, B. Corraze, M. Querré, P. Stoliar, M. Rozenberg, T. Cren, D. Roditchev, V. T. Phuoc, M.-P. Besland, and L. Cario, *Adv. Funct. Mater.* **25**, 6287 (2015).
- [24] M. Imada, A. Fujimori, and Y. Tokura, *Rev. Mod. Phys.* **70**, 1039 (1998).
- [25] P. Limelette, A. Georges, D. Jérôme, P. Wzietek, P. Metcalf, and J. M. Honig, *Science* **302**, 89 (2003).
- [26] J. Zhang, A. S. McLeod, Q. Han, X. Chen, H. A. Bechtel, Z. Yao, S. N. Gilbert Corder, T. Ciavatti, T. H. Tao, M. Aronson, G. L. Carr, M. C. Martin, C. Sow, S. Yonezawa, F. Nakamura, I. Terasaki, D. N. Basov, A. J. Millis, Y. Maeno, and M. Liu, *Phys. Rev. X* **9**, 011032 (2019).
- [27] J. Bertinshaw, N. Gurung, P. Jorba, H. Liu, M. Schmid, D. T. Mantadakis, M. Daghofer, M. Krautloher, A. Jain, G. H. Ryu, O. Fabelo, P. Hansmann, G. Khaliullin, C. Pfleiderer, B. Keimer, and B. J. Kim, *Phys. Rev. Lett.* **123**, 137204 (2019).
- [28] C. Sow, R. Numasaki, G. Mattoni, S. Yonezawa, N. Kikugawa, S. Uji, and Y. Maeno, *Phys. Rev. Lett.* **122**, 196602 (2019).
- [29] H. Fukazawa, S. Nakatsuji, and Y. Maeno, *Physica B* **281-282**, 613 (2000).
- [30] M. Sakaki, N. Nakajima, F. Nakamura, Y. Tezuka, and T. Suzuki, *J. Phys. Soc. Jpn.* **82**, 093707 (2013).
- [31] C. S. Alexander, G. Cao, V. Dobrosavljevic, S. McCall, J. E. Crow, E. Lochner, and R. P. Guertin, *Phys. Rev. B* **60**, R8422 (1999).
- [32] Q. Han and A. Millis, *Phys. Rev. Lett.* **121**, 067601 (2018).
- [33] D. I. Khomskii, *Transition Metal Compounds* (Cambridge University Press, Cambridge, 2014).